HHS Public Access

Author manuscript

Phys Med Biol. Author manuscript; available in PMC 2024 August 14.

Published in final edited form as:

Phys Med Biol. ; 68(17): . doi:10.1088/1361-6560/acea17.

Evaluation of the feasibility of a multi-source CBCT for maxillofacial imaging

Shuang Xu[1], **Boyuan Li**[2], **Christina R. Inscoe**[2], **Daniel Bastawros**[2], **Donald A. Tyndall**[3], **Yueh Z. Lee**[4], **Jianping Lu**[2], **Otto Zhou**[2]

[1]Department of Applied Physical Sciences, University of North Carolina at Chapel Hill; Chapel Hill, NC 27599, USA.

[2]Department of Physics and Astronomy, University of North Carolina at Chapel Hill; Chapel Hill, NC 27599, USA.

[3]Department of Diagnostic Sciences, Adams School of Dentistry, University of North Carolina at Chapel Hill; Chapel Hill, NC 27599, USA.

[4]Department of Radiology, University of North Carolina at Chapel Hill; Chapel Hill, NC 27599, USA.

Abstract

Objective: The aim of this study was to investigate the feasibility of improving the image quality and accuracy of cone beam computed tomography (CBCT) by replacing the conventional wide cone angle X-ray tube with a distributed X-ray source array positioned in the axial direction.

Approach: The multisource CBCT (ms-CBCT) design was experimentally simulated using a benchtop scanner with a carbon nanotube (CNT) X-ray tube and a flat-panel detector. The source was collimated and translated in the axial direction to simulate a source array with a reduced cone angle for each beam. An adjacent scatter ratio subtraction (ASRS) method was implemented for residual scatter reduction. Several phantoms were imaged using the ms-CBCT and conventional CBCT configurations under otherwise similar conditions. The requirements of the ms-CBCT design on the X-ray source and detector were evaluated.

Main results: Compared to the conventional CBCT, the ms-CBCT design with 8 sources and ASRS significantly improved the image quality and accuracy, including: 1) reducing the cupping artifact from 15% to 3.5%; 2) reducing the spatial nonuniformity of the CT Hounsfield unit (HU) values from 38.0 to 9.2; 3) improving the contrast-to-noise ratio of the low contrast objects (acrylic and low density polyethylene inserts) against the water-equivalent background by ~20% and 4) reducing the root-mean-square error of the HU values by 70%, from 420.1 to 124.4. The imaging dose and scanning time used by the current clinical CBCT for maxillofacial imaging can be achieved by current source and detector technologies.

Significance: The ms-CBCT design significantly reduces the scatter and improves the image quality and accuracy compared to the conventional CBCT.

zhou@email.unc.edu .

Keywords

CBCT; maxillofacial imaging; scatter; HU value accuracy; contrast; multiple X-ray sources; carbon nanotube X-ray source

1. Introduction

Cone beam computed tomography (CBCT) provides a three-dimensional (3D) representation of an object with isotropic resolution at a relatively low cost and low radiation dose. With a flat panel detector (FPD) and conical geometry radiation, an entire volumetric dataset is acquired with a single rotation of the gantry, eliminating the need for patient translation. CBCT has found widespread applications in dentistry[1–3] and growing areas of medicine[4]. The large imaging volume however results in strong scatter and a high scatter-primary-ratio (SPR) that can exceed 100%[5–7]. The strong scatter reduces the contrast resolution compared to the multi-detector CT (MDCT)[5,8], limiting the clinical applications of CBCT to primarily imaging bone structures. The CT Hounsfield Unit (HU) values derived from CBCT are known to be inaccurate and spatially nonuniform due to the strong scatter and beam hardening, making it challenging for quantitative analysis such as measuring the bone mineral density for evaluation of the bone quality for implant planning. The wide cone beam also leads to significant cone beam artifacts in the reconstructed images.

Many hardware and software-based methods have been proposed to either suppress or correct scatter in CBCT with varying degrees of success[9]. Anti-scatter grid reduces the scatter intensity but also the primary photons thus increases the imaging dose[10]. Some scatter correction algorithms based on the beam stop array were used to estimate and reduce the scatter but require additional projection acquisitions[11–15]. Postprocessing scatter correction techniques have also been investigated extensively, but a practical scatter correction method which is patient-specific remains elusive. The inverse geometry CT[16,17] and the tetrahedron-beam CT[18] are effective in scatter reduction, but the X-ray photon fluxes required are difficult to achieve.

CT architectures using either multiple individual X-ray tubes or a linear source array arranged in the axial direction of the scanner have been explored previously. Yin et al. considered various acquisition schemes using multiple longitudinally placed sources[19]. Ying and coworkers[20] disclosed a CT design using a longitudinally placed X-ray source array with the radiation from each source covering the entire detector array. We previously described a multisource approach using a linear carbon nanotube (CNT) X-ray source array along the axial direction[21]. Gang et al. reported a prototype extremity CBCT scanner using 3 individual X-ray tubes, each illuminating the entire field of view (FOV) and demonstrated improved image quality in the axial direction[22]. In this design, each source still has a large cone angle as a single source CBCT. Becker and colleagues[23] evaluated several multisource CBCT configurations by Monte Carlo simulation and demonstrated significantly improved image quality along the axial direction and reduced SPR for the collimated multisource axial scan configuration in a physical simulation using a single source breast CBCT scanner.

The purpose of this study was to investigate the feasibility of the multi-source CBCT (ms-CBCT) design specifically for maxillofacial imaging. Although either an assembly of individual X-ray tubes or a distributed X-ray source array using various types of electron emitting cathodes can in principle be employed for this purpose, a CNT-based field emission X-ray source array[24,25] was chosen for several reasons. A distributed X-ray source array in general affords a smaller inter-focal spot spacing compared to an assembly of off-the-shelf X-ray tubes. X-ray exposure from a field emission source can be rapidly switched with an instantaneous response[25]. Both properties are necessary for the ms-CBCT design. In addition, the CNT X-ray source arrays are now manufactured commercially.

2. Methods and materials

2.1 Proposed ms-CBCT imaging configuration

The ms-CBCT replaces the single X-ray source in a CBCT with a linear CNT X-ray source array with multiple focal spots ("sources"), aligned along the axial direction of the scanner, as shown in Figure 1a. The radiation from each source is collimated to a narrow cone angle. For each X-ray exposure, a segment of the object is imaged and recorded on a corresponding section of the FPD. Any scattered photon received outside this detector area is rejected. For CT imaging the N_{source} number of collimated sources are electronically scanned across the object N_{view} times following the timing diagram shown as the gantry rotates around the object by either 180 + fan angle or 360 degrees as in a conventional CBCT. All together $N_{source} \times N_{view}$ projection images are collected during one full gantry rotation. In this design, the ROI can be adjusted electronically by choosing a subset of the sources for imaging.

2.2 Benchtop testing system

This study was carried out using a benchtop system consisting of a CNT field emission X-ray source and a flat panel detector mounted on a rotating gantry (Model 430, Huber GmbH, Germany), as shown in Figure 2a. To have the flexibility of investigating various source array configurations, a source with a single focal spot was used. It was placed on a motorized translation stage (Velmex, Inc., Bloomfield, NY, USA) and translated in the axial direction to N_{source} (number of x-ray sources) locations over an 84 mm linear span. An external collimator was placed outside the X-ray window to define the X-ray beam fan (ϕ) and cone (θ) angles. Pulsed X-ray radiation was generated by pulsing the voltage applied between the gate electrode and the CNT cathode at a constant anode voltage. The X-ray focal spot size was adjusted electronically by changing the voltage applied to the electrostatic focusing electrode to the size of IEC1.0[26].

The detector is a CMOS flat panel detector with a CsI scintillator designed for dental CBCT, with an active area of 147.1 mm (width) × 113.7 mm (height) and a pixel pitch of 99um (Xineos-1511, Teledyne DALSA, Waterloo, CA). It can be operated at 86 frames per second (fps) in 2×2 binning mode and up to 300fps in the region of interest (ROI) mode. In this study, the 2×2 binning mode was used. The detector integration and X-ray exposure were triggered by external triggering signals. A computer interface was written in LabVIEW (National Instruments, Austin, TX) to automate the image acquisition process.

The source-object-distance (SOD) and source-imager-distance (SID) were 400 mm and 615 mm, respectively, similar to those of a commercial dental CBCT scanner. With this geometry, the FOV is 96 mm (width) × 100 mm (height) at the rotation axis, comparable to that of a medium FOV dental CBCT scanner[27]. This is however insufficient to cover the width of a human head, resulting in data truncation errors. To extend the FOV, the detector was shifted laterally by 70 mm to provide an effective FOV of 187 mm (width) × 100 mm (height), as illustrated in Figure 2b. The detector offset CBCT geometry has been investigated in the past[28–31] and implemented in several commercial dental CBCT systems[32] and a prototype breast CBCT[33]. The geometry of the ms-CBCT scanner was calibrated by measuring a phantom with two stainless steel beads embedded in an acrylic slab, following the method described by Yang et al.[34].

A 160 mm diameter uniform cylinder fabricated using the SolidWater material (Sun Nuclear Co, Melbourne FL), an anthropomorphic adult skull and tissue-equivalent head phantom (RANDO – radiation analogue dosimetry system; Nuclear Associates, Hicksville, NY), and a homemade contrast phantom were imaged using the benchtop scanner at variable system configurations. The homemade contrast phantom consists of a 160 mm diameter and 40 mm thick SolidWater disk with four 19 mm diameter wells filled with acrylic, low-density polyethylene (LDPE), air, and Macor (machinable ceramic) sandwiched between uniform SolidWater cylinders of the same diameter.

2.3 ms-CBCT imaging protocol

The ms-CBCT imaging configuration was experimentally simulated by translating the X-ray source in the axial direction to N_{source} positions ($N_{source} = 1$ for N1 and $N_{source} = 8$ for N8) over an 84 mm span to simulate a source array with N_{source} focal spots with the same linear span. For the N8 configuration, the vertical width of the collimator, therefore the beam cone angle (θ), was fixed at 2.3° to ensure overlapping of the X-ray beams from the two adjacent sources at the entrance surface of the object based on the relation:

$$\tan\left(\frac{\theta}{2}\right) = \frac{\Delta S}{2(SOD - r)}$$

Where r is the radius of the object, which was assumed to be 100 mm, SOD = 400 mm, and ΔS is the inter-source spacing in the axial direction. By measuring the blank images of the collimated beams, the illuminated detector region for each source was determined for data preprocessing and reconstruction. The cone angle was fixed at 10.3° for the N1 configuration, and the fan angle (defined by the horizontal width of the collimator) was fixed at 13.5° to allow the X-ray photons to illuminate the entire X-ray detector width (147.1 mm) with a 70mm detector offset distance. For each axial source position, 360 projection images were collected during a 360 degrees gantry rotation.

The X-ray source was operated at 90 kVp and 5 mA tube current, which are the values commonly used in dental CBCT[27]. The X-ray source has a 2 mm inherent Al filtration. Additional Cu filtration was added. The cupping artifact was measured using both 0.1 mm Cu and 0.5 mm Cu filtration. The rest of the imaging studies in this paper were performed

using 0.5 mm Cu. The total half-value-layer (HVL) was 4.6mm Al for the case of 0.1 mm Cu + 2 mm Al (inherent), and 8.2 mm Al for 0.5 mm Cu + 2 mm Al (inherent). The exposure time per view/pulse 13 ms resulting in 23.4 mAs for 0.1 mm Cu filtration, and 20 ms resulting in 36 mAs for 0.5 mm Cu filtration.

2.4 Adjacent scattering ratio subtraction (ASRS) and CT image reconstruction

The ms-CBCT imaging geometry further presents an opportunity to estimate and subtract the residual scatter through post-processing. Since the primary photons I_p from each collimated beam illuminate only a section of the detector, the residual scatter I_s in the illuminated area (marked blue) can be estimated from the scatter signal I_s' recorded on the adjacent director rows not illuminated by the primary beam (marked green), as illustrated in Figure 3. To avoid contamination from the tail of the primary beam, a section of the detector 50 mm away from the central line of the illuminated area was used in this study to obtain the scatter signal I_s' as a function of the detector column number. The value was averaged over 50 adjacent detector rows at the same column in the green region. The adjacent scatter ratio r was calculated by $I_s'/(I_p + I_s)$ for each column. A spline function was used to fit the raw data to obtain the smoothed scatter ratio r'. The primary photons I_p was then estimated by applying $(I_p + I_s)(1 - r')$. The same r' function was used for all detector rows in the directly illuminated region to subtract the residual scatter. The same process was applied to all projections from all sources.

By estimating I_S using I_s', the residual scatter in small cone angle configurations can be further reduced. Similar approaches were applied in previous studies and were found to be effective in reducing scatter and enhancing the CNR[35,36].

The processed projection images from all source positions were used to reconstruct volumetric CT images using an iterative reconstruction (IR) algorithm based on the ASTRA Toolbox[37,38]. All $360 \times N_{source}$ projection views were included in one single system matrix, including the distinct source/detector geometry for each projection view. The iso-center of the whole CT system was located at the center of the region of interest (ROI). The 3D Simultaneous Iterative Reconstruction Technique (SIRT) was used to reconstruct the volume of interest. The whole CT reconstruction process was implemented in the MATLAB R2022a environment on a PC with Intel Core i5-9600K CPU @ 3.70GHz and an NVIDIA GeForce RTX 2070 graphic card. The parameters for the reconstruction were 360 projection views from 0 to 2π, $0.5 \times 0.5 \times 0.5\ mm^3$ voxel size ($0.25 \times 0.25 \times 0.25\ mm^3$ for the RANDO head phantom), and 150 iterations of SIRT.

2.5 Clinical CBCT and MDCT

The same phantoms were also imaged by two clinical dental CBCT systems (3D Accuitomo 170, Morita, Japan and CS9300, Carestream Dental, US) and a multidetector CT (SOMATOM Force, Siemens, Germany). All scanners were operated at 90 kVp. For the 3D Accuitomo 170 CBCT scanner, the standard clinical protocol was used, which was: full 360° gantry rotation, 170 mm × 120 mm FOV, continuous X-ray radiation, 6 mA tube current, 105 mAs, dose-area-product (DAP) of $30.7\ dGy \cdot cm^2$, a measured HVL thickness

of 5.5 mm Al and $0.33 \times 0.33 \times 0.33\ mm^3$ voxel size. For the CS9300 scanner, the standard clinical protocol for large FOV adult patient was used, which was: partial gantry rotation, 170 mm × 130 mm FOV, pulsed X-ray radiation, 5 mA tube current, 56 mAs, DAP of $19.8\ dGy \cdot cm^2$, 2.5 mm Al + 0.1 mm Cu filtration and $0.3 \times 0.3 \times 0.3\ mm^3$ voxel size. For the MDCT scanner (Siemens SOMATOM Force), the imaging parameters were: 90 kVp, 85 mA, 100 mAs, $CTDI_{vol} = 6.2\ mGy$, 0.6 mm Sn filter (simulated HVL of 8.5 mm Al using the open source software Spektr[39]), WEDGE_2 filter, $0.35 \times 0.35 \times 0.6\ mm^3$ voxel size, Uh36u convolution kernel and without ADMIRE algorithm. The images were processed and reconstructed using commercial softwares from the manufacturers. The CS9300 scanner in our institution malfunctioned during the study, resulting in an incomplete dataset that only includes the Rando phantom. There exists a multitude of setting differences between the ms-CBCT benchtop system and clinical CBCT, all clinical scanning results were treated as representative performances of currently available clinical CBCT.

2.6 Scatter and scatter-primary-ratio

The scatter intensity I_S and the SPR in the projection images of the cylindrical SolidWater phantom were measured based on a procedure described by Johns and Yaffe[5,40], as illustrated in Figure 4a. A 20 mm diameter and 5 mm thick Pb disk was placed in front of the phantom, which was sufficient to block all the primary photons. Any photons recorded directly behind the beam blocker were the scatter intensity I_s. Projection images were recorded at different X-ray beam cone angles by changing the opening width of the collimator in the axial direction. The beam fan angle was kept at 13.6° to illuminate the entire detector without offset. The intensity of the transmitted primary beam I_p was calculated by subtracting the I_s from $(I_p + I_s)$. Instead of taking a separate set of images without the beam blocker, the $(I_p + I_s)$ was estimated from the photon intensity adjacent to the blocked area in the axial direction. The SPR was then computed as $SPR = I_s / I_p$.

2.7 Uniformity of the CT numbers

The cupping artifact was evaluated by analyzing the line profile of the central axial slices of the homogenous cylindrical SolidWater phantom and the anthropomorphic head phantom. The degree of cupping artifact (t_{cup}) was quantified by computing:

$$t_{cup} = 100 \times \frac{\mu_{max} - \mu_{min}}{\mu_{max}}$$

Where μ_{max} and μ_{min} are the maximum and minimum values of the measured linear attenuation coefficients, respectively. The phantom was imaged first using 0.1 mm Cu filtration and then using 0.5 mm Cu filtration.

The spatial uniformity of the CT HU values was quantified by measuring the variation in the CT HU mean values derived from 9 different ROIs on the axial plane of the SolidWater part of the homemade contrast phantom. The CT numbers of all reconstructions under different configurations were calibrated according to Gammex CT ACR 464 phantom testing instruction[41].

2.8 Contrast and Contrast-to-noise ratio

The contrast and contrast-to-noise ratio (CNR) of the low-contrast acrylic and LDPE against the SolidWater background were measured from the reconstructed CT image of the contrast phantom. As shown in Figure 8d, the mean HU values over the selected 10 mm × 10 mm ROIs (solid squares in Figure 8d) of the acrylic and LDPE inserts were obtained. For the SolidWater background, in order to decouple the impact of the cupping effect, four 10 mm × 10 mm ROIs were chosen to obtain averaged SolidWater background HU values and standard deviations. These nearby ROIs have the same radius as the ROIs of acrylic and LDPE (dashed squares in Figure 8d, two of them used for each insert). The CNR was computed as the absolute HU value difference between the contrast insert and SolidWater background divided by the standard deviation of the SolidWater background.

2.9 Accuracy of the CT HU values

Four 10 mm × 10 mm ROIs and one 40 mm × 40 mm ROI (solid squares in Figure 8d) were selected to measure the HU values of four different inserts and SolidWater respectively. The HU values derived from the MDCT scanner were used as the ground truth for comparison.

2.10 Imaging dose and the scanning time estimation

The x-ray dose rate was measured using a dose meter (Raysafe X2, Unfors Raysafe AB, Sweden) placed at the center of the detector surface that was directly illuminated by the primary beam without the object. The total image dose-area-product (DAP), a parameter commonly used to characterize the radiation in a CBCT, was calculated for the ms-CBCT using the measured dose rate by:

$$DAP = D_p \times L_w \times L_h \times N_{view} \times N_{source}$$

where, D_p is the dose per X-ray pulse measured at the center of the detector surface, L_w and L_h are the width and height of the directly illuminated area of the detector, N_{view} is the number of projection views and N_{source} is the number of sources. L_w is the detector width, and L_h is decided by the full width at half maximum (FWHM) of the beam intensity profile in the vertical direction.

The total scan time T_{scan} for the intended ms-CBCT design with a source array operating in the sequential imaging scheme was estimated by:

$$T_{scan} = (t_{exposure} + t_{readout}) \times N_{view} \times N_{source}$$

where, $t_{exposure}$ and $t_{readout}$ are respectively the X-ray exposure time per view/pulse and the detector readout time.

3. Results

3.1 Scatter and SPR

Figure 4b shows the SPR values measured from the 16 cm diameter SolidWater phantom using X-ray beams with different cone angles. The SPR essentially decreased with an increasing number of X-ray sources (decreasing cone angle), from 47% in N1 ($\theta = 10.3^{\circ}$) to 20% in N8 ($\theta = 2.3^{\circ}$), while the fan angle was kept at 13.6° to illuminate the detector without offset. At the smallest cone angle studied ($\theta = 0.8^{\circ}$) the SPR was 13%. This result was expected. The more X-ray sources used for the same FOV, the smaller the imaging volume for each source, and therefore the lower the scatter intensity.

3.2. Spatial uniformity

The normalized linear attenuation coefficients of the homogeneous SolidWater phantom in the central axial plane were plotted as a function of the position for three ms-CBCT configurations, all with the same 0.1 mm Cu filtration, in Figure 5a. For N1 ms-CBCT, whose geometry is similar to a clinical dental CBCT, a large variation in the normalized attenuation (15%) is observed in the line profiles.

The CT cupping artifact decreased from 15% in N1 to 10% in N8. Further increasing the number of sources did not result in a meaningful improvement in reducing the cupping artifact. By applying the ASRS method, the severity of the artifact was further reduced to 7.5% in N8* (* denotes the application of the ASRS method). The residual nonuniformity is attributed to the beam hardening effect and in-plane scatter. The effect of beam hardening is demonstrated in Figure 5b which compares the line profiles for the N8* configuration with 0.1 mm and 0.5 mm Cu filtration. At increased mean energy, the cupping artifact was reduced further from 7.5% to 3.5% in N8*.

For reference, the results from the same phantom imaged using a clinical CBCT scanner (3D Accuitomo 17, Morita) at the same kVp were also plotted in the same figure. As expected, the clinical CBCT showed a severe cupping artifact, at the magnitude comparable to the N1 configuration, at the same kVp and similar beam quality (HVL of 5.5 mm Al for the clinical scanner and HVL of 4.6 mm Al for N1 with 0.1 mm Cu). The artifact was reduced significantly in the ms-CBCT design with 8 sources.

The 9 different ROI positions covering the SolidWater part on the axial plane of the contrast phantom chosen for characterizing the HU spatial nonuniformity are shown in Figure 6. For the clinical dental CBCT (3D Accuitomo 170, Morita), the Greyscale Values (GV) were used because most of the CBCT scanners including the ones used in this study only provide the GV instead of HU values. The standard deviation in the mean HU values of these ROIs decreased from 38.0 in N1, to 19.8 in N8, and to 9.2 in N8*.

Figure 7 shows axial CT images and the corresponding line profiles of the RANDO head phantom scanned using two clinical dental CBCT scanners and the benchtop ms-CBCT in the N8* configuration. As shown, the uniformity of HU values in the region (red dashed rectangle) of the phantom with homogeneous materials was improved significantly in the

N8* configuration compared with the GV line profiles from the clinical CBCT scanners. In addition, the obvious shading artifacts around the teeth and bones in both clinical CBCTs were also reduced in the N8* configuration due to substantial scatter reduction.

3.3. Contrast and Contrast-to-noise ratio

Figure 8 shows the axial CT slices of the contrast phantom imaged using a clinical dental CBCT (3D Accuitomo 170, Morita), N1 and N8* ms-CBCT. The same filtration was used for both the N1 and N8* configurations. It can be seen that the background is darker in the middle than the peripheral of the axial slice in the clinical CBCT and N1 ms-CBCT due to the strong cupping artifact. As expected, the background is more uniform in the N8* image. In addition, the artifact caused by the strong attenuating ceramic insert in the clinical CBCT and N1 images is no longer apparent in the N8* image. The contrast between the low-contrast acrylic and the SolidWater was 75.7 HU in the N1 and increased to 92.1 HU in N8* image. Similarly, the contrast between LDPE and the SolidWater increased from 96.0 HU to 117.4 HU. These represent a 21.5% and 22.3% improvement, respectively. The CNR increased from 1.53 to 1.84 for the acrylic and 1.99 to 2.39 for the LDPE with respect to the SolidWater background, corresponding to a 19.9% and 20.6% increase, respectively.

3.4. Accuracy of the CT HU values

The HU values of the inserts and the SolidWater of the contrast phantom were measured by averaging over the ROIs in the central axial plane for the mean values and standard deviations, as shown in Figure 8d. The values are listed in Table 1. The HU values of the same phantom measured using the clinical MDCT scanner are listed and used as the reference. As shown, the HU values derived from the N1 ms-CBCT deviate considerably from the reference values from the MDCT. The accuracy of the HU values from the N8* ms-CBCT is significantly improved compared with the N1 ms-CBCT. The root-mean-square error (RMSE) of the HU values, using MDCT results as the reference, was reduced from 420.1 in N1 to 124.4 in N8* representing a 70% reduction. The results from a clinical CBCT scanner (3D Accuitomo 17, Morita) were also included for comparison as a representative performance of currently available clinical CBCT. Because of the inherent HU value inaccuracy of CBCT, the commercial system only reports the GV value instead of the HU value.

3.5. Imaging dose and scanning time

The dose rate at 90 kVp with 0.1 mm Cu is $0.184\ mGy/mAs$. The DAP for the N8 ms-CBCT configuration ($N_{source} = 8$, $L_w = 147.1$ mm, $L_h = 32.5$ mm, and $N_{view} = 360$) was calculated to be $16.5\ dGy \cdot cm^2$, giving a total imaging dose of $10.2\ mGy$ at the rotation center. The total imaging DAP and dose is similar to the values of the two clinical dental CBCT scanners for the same phantom, which were $30.7\ dGy \cdot cm^2$ and $15.0\ mGy$ for the 3D Accuitomo 170, and $19.8\ dGy \cdot cm^2$ and $9.0\ mGy$ for CS9300. For N1 ms-CBCT with 0.1mm Cu filter, the DAP is $7.2\ dGy \cdot cm^2 \left(10.2\ mGy\right)$. For the 0.5mm Cu filtration, the DAP for N1 and N8 configurations are $3.1\ dGy \cdot cm^2 \left(4.3\ mGy\right)$ and $7.0\ dGy \cdot cm^2 \left(4.3\ mGy\right)$ respectively.

The total scanning time for the imaging protocol of 90 kVp and 23.4 mAs over 360 views was estimated to be 70.8 s with the exposure parameters of 5 mA tube current, 13 ms exposure time per view/pulse and 11.6 ms detector readout time (2×2 binning mode).

4. Discussion

The results of this study demonstrate that the ms-CBCT design reduces scatter and scatter-primary-ratio, which is consistent with the results from previous studies of scatter in CBCT[5,6,42]. For example, Yang reported an increasing SPR from less than 10% to ~30% for a 15 cm diameter water phantom as the collimator slit width was increased in a conventional dental CBCT scanner[6]. Pauwels and coworkers[42] showed a large increase in the SPR when the FOV was increased from 6 cm×6 cm to 17 cm×12 cm. Most of the residual scatter in small cone angle cases is attributed to the scatter within the fan beam. The ms-CBCT design also increases the spatial uniformity and accuracy of the CT HU values compared with conventional CBCT configuration.

Overall these improved performances compared with conventional CBCT are expected from imaging physics considerations because of the reduced imaging volume per source when the single X-ray beam with a large cone angle is replaced with multiple narrowly collimated X-ray beams. The ms-CBCT design is essentially multiple axial CT stacked in the axial direction. This data acquisition scheme also enabled the implementation of an effective adjacent scatter ratio subtraction method to estimate and remove the residual in-plane scatter to enhance image quality and accuracy.

The design however requires significantly more image frames compared to a conventional CBCT. A key question for potential clinical applications is whether an acceptable imaging time can be achieved at the required imaging dose. The present benchtop study used an older generation CNT X-ray source with limited output power and an off-the-shelf FPD to demonstrate the feasibility of the ms-CBCT concept. The imaging time estimated using the parameters of these two components is substantially longer than that of a typical scanning time of medium and large FOV dental CBCT, which is 20–30 s[43]. There are several options to reduce the T_{scan} of the ms-CBCT, including increasing the X-ray source output and/or reducing the $t_{readout}$. With advancements in the manufacturing technologies, newer generation of CNT X-ray source arrays can operate at a significantly higher output power than the source used in this study. A fixed anode source array operating at 15 mA and up to 110 kVp at the focal spot size and duty cycle required for ms-CBCT has recently been reported, with long-term stability[44]. Increasing the X-ray tube current to 15mA under otherwise the same conditions will reduce the scanning time to 45.9 s. Further reduction can be achieved by increasing the detector readout speed. Instead of reading out the entire detector for each exposure, a region of interest (ROI) mode can be used to read only the detector rows illuminated by the primary photons. For the current FPD technology, the $t_{readout}$ is directly proportional to the number of readout rows. The ROI mode substantially reduces $t_{readout}$. For example, the detector used in this study can be operated at 300 fps ($t_{readout}$ = 3.3 ms) in the ROI mode using 100 detector rows without binning. Another option is to use an wider FPD to cover the entire FOV without the offset, which will essentially double the DAP at the same X-ray exposure. By combining the reduced readout time and exposure time, the T_{scan} of an

N8 ms-CBCT scan can be reduced to below 20s, comparable to that of the current clinical dental CBCT.

The intensity line profile from the benchtop scanner showed two distinct minimums at ±25 mm from the center of the cylinder. This is different from the line profile measured from a typical CBCT scanner without the detector offset where a single minimum point at the center of the cylinder is commonly observed[5]. The presence of the double minimum is attributed to the asymmetric beam collimation (with respect to the effective FOV) used to ensure the X-ray photons illuminate only the portion of the object contributing to image formation in the detector offset geometry. As a result, the point with the highest scatter intensity is no longer at the center of the cylinder, but at some distance away from it for each projection view. For a CT scan with 360° gantry rotation the points with the highest scatter intensity, therefore the lowest apparent attenuation coefficient, form a ring around the center axis of the cylinder. The line profile intercepts the ring at two points, resulting in the double minimum observed. This was verified experimentally. Opening the fan beam collimation to allow full coverage of the phantom removed the two minimums and resulted in a line profile with a single minimum at the center of the cylinder. A similar double minimum line profile was also observed in a recent study of scatter in a CBCT with offset detector[45].

In the current design, the photons from the adjacent X-ray beams intercept at the object entrance surface to ensure sufficient coverage and the quality of the CT images. This results in partial overlap of the radiation and increased radiation dose in the overlap regions of the object along the axial direction, which is similar to the situations of an axial CT scan with a small pitch[46]. The nonuniformity of the dose distribution can potentially be minimized by adding a flat field filter in front of the object.

Finally, based on the results from this study, a prototype ms-CBCT scanner with a dedicated CNT X-ray source array has been assembled and is currently under evaluation for maxillofacial imaging.

5. Conclusion

This study demonstrates that the scatter and scatter-primary-ratio of a CBCT scanner can be significantly reduced, and the spatial uniformity and accuracy of the CT HU values can be improved by replacing the regular single source X-ray tube with an array of multiple X-ray sources in the axial direction to reduce the beam cone angle of each source. The ms-CBCT design requires more image frames. For maxillofacial imaging evaluated in this study, a clinically acceptable ms-CBCT scanning time can be achieved using the current CNT X-ray source array and detector technologies. A dedicated CNT X-ray source array designed based on the results from this study has been fabricated and the work is in progress to characterize a prototype ms-CBCT for maxillofacial imaging.

Acknowledgements

We thank Dr. Enrique Platin for helpful discussions. We thank Amber Dodson, Rose Saulsbury, Emily Rogers, Courtney Wrenn, Chanetha McCabe and Jane Isley at the Oral Radiology Clinic and Dr. Adam Kimple and Dana St Pierre at the ENT Clinic of UNC for the technical assistance.

Disclosure:

The work was partially supported by NIH under Grant R56DE030962-01 and NC Biotechnology Center award 2021-TRG-6725. Otto Zhou has equity ownership and serves on the board of directors of XinVisio, LLC., to which the technologies used or evaluated in this project have been licensed. Jianping Lu has equity ownership in XinVisio, LLC.. Zhou, Lu, Inscoe, and Lee are co-inventors of licensed technology evaluated in this study. All activities have been approved by the institutional COI committee.

References

1. Gaêta-Araujo H et al. Cone beam computed tomography in dentomaxillofacial radiology: a two-decade overview. Dentomaxillofac Radiol 49, 20200145, doi:10.1259/dmfr.20200145 (2020). [PubMed: 32501720]
2. Tyndall DA & Rathore S Cone-beam CT diagnostic applications: caries, periodontal bone assessment, and endodontic applications. Dent Clin North Am 52, 825–841, vii, doi:10.1016/j.cden.2008.05.002 (2008). [PubMed: 18805231]
3. Scarfe WC & Angelopoulos C (Springer, 2017).
4. Siewerdsen JH in Computed Tomography (eds Samei E & Pelc NJ) (Springer Nature Switzerland, 2020).
5. Siewerdsen JH & Jaffray DA Cone-beam computed tomography with a flat-panel imager: Magnitude and effects of x-ray scatter. Med. Phys 28, 220 (2000).
6. Yang CC Characterization of Scattered X-Ray Photons in Dental Cone-Beam Computed Tomography. PLoS One 11, e0149904, doi:10.1371/journal.pone.0149904 (2016). [PubMed: 26950435]
7. Schulze R et al. Artefacts in CBCT: a review. Dentomaxillofac Radiol 40, 265–273, doi:10.1259/dmfr/30642039 (2011). [PubMed: 21697151]
8. Angelopoulos C, Scarfe WC & Farman AG A Comparison of Maxillofacial CBCT and Medical CT. Atlas Oral Maxillofacial Surg Clin N Am 20, 1–17 (2012).
9. Tang X, Krupinski EA, Xie H & Stillman AE On the data acquisition, image reconstruction, cone beam artifacts, and their suppression in axial MDCT and CBCT - A review. Med Phys, doi:10.1002/mp.13095 (2018).
10. Kyriakou Y & Kalender W Efficiency of antiscatter grids for flat-detector CT. Phys Med Biol 52, 6275–6293, doi:10.1088/0031-9155/52/20/013 (2007). [PubMed: 17921585]
11. Ning R, Tang X & Conover D X-ray scatter correction algorithm for cone beam CT imaging. Med Phys 31, 6275–6293, doi:10.1118/1.1711475 (2004).
12. Sechopoulos I X-ray scatter correction method for dedicated breast computed tomography. Med Phys 39, 2896–2903, doi:10.1118/1.4711749 (2012). [PubMed: 22559662]
13. Yang K, Burkett G & Boone JM A breast-specific, negligible-dose scatter correction technique for dedicated cone-beam breast CT: a physics-based approach to improve Hounsfield Unit accuracy. Phys Med Biol 59, 6487–6505, doi:10.1088/0031-9155/59/21/6487 (2014). [PubMed: 25310586]
14. Zhu L Local filtration based scatter correction for cone-beam CT using primary modulation. Med Phys 43, 6199, doi:10.1118/1.4965042 (2016). [PubMed: 27806607]
15. Lee H, Fahimian BP & Xing L Binary moving-blocker-based scatter correction in cone-beam computed tomography with width-truncated projections: proof of concept. Phys Med Biol 62, 2176–2193, doi:10.1088/13616560/aa5913 (2017). [PubMed: 28079527]
16. Schmidt TG et al. A prototype table-top inverse-geometry volumetic CT system. Medical Physics 33, 1867 (2006). [PubMed: 16872094]
17. Neculaes VB et al. Multisource inverse-geometry CT. Part II. X-ray source design and prototype. Med Phys 43, 4617, doi:10.1118/1.4954847 (2016). [PubMed: 27487878]
18. Zhang T, Schulze D, Xu X & Kim J tetrahedron beam computed tomography(TBCT): a new design of volumetric CT system. Physics in Medicine and Biology 54, 3365 (2009). [PubMed: 19430106]
19. Yin Z, de Man B & Pack J 3D Analytic Cone-Beam Reconstruction for Multiaxial CT Acquisitions. International Journal of Biomedical Imaging 2009, 538389 (2009). [PubMed: 19730750]

20. Ying Z, Simanovsky S, Naidu R & Marcovici S US 8,995,610, CT scanning systems and methods using multipixel X-ray sources. (2015).
21. Zhou O et al. U.S. Patent 7,082,182, “Computed tomography system for imaging of human and small animal”. (2006).
22. Gang GJ et al. Image quality and dose for a multisource cone-beam CT extremity scanner. Med Phys 45, 144–155, doi:10.1002/mp.12659 (2018). [PubMed: 29121409]
23. Becker AE, Hernandez AM, Schwoebel PR & Boone JM Cone beam CT multisource configurations: evaluating image quality, scatter, and dose using phantom imaging and Monte Carlo simulations. Phys Med Biol 65, 235032, doi:10.1088/1361-6560/abc306 (2020). [PubMed: 33080583]
24. Zhang J et al. A stationary scanning x-ray source based on carbon nanotube field emitters. Appl. Phys. Lett 86, 184104 (2005).
25. Inscoe C, Lee Y, Lu J & Zhou O in Nanostructured Carbon Electron Emitters and Applications (ed Saito Yahachi) (Jenny Stanford Publishing Pte Ltd, 2020). Saito) (Jenny Stanford Publishing Pte Ltd, 2020).
26. IEC 60336:2020 https://webstore.iec.ch/publication/62504.
27. Ludlow JB et al. Effective dose of dental CBCT-a meta analysis of published data and additional data for nine CBCT units. Dentomaxillofac Radiol 44, 20140197, doi:10.1259/dmfr.20140197 (2015). [PubMed: 25224586]
28. Cho PS, Rudd AD & Johnson RH Cone-beam CT from width-truncated projections. Comput Med Imaging Graph 20, 49–57, doi:10.1016/0895-6111(96)00031-6 (1996). [PubMed: 8891422]
29. Wang G X-ray micro-CT with a displaced detector array. Med Phys 29, 1634–1636, doi:10.1118/1.1489043 (2002). [PubMed: 12148746]
30. Li L, Chen Z, Zhang L, Xing Y & Kang K A cone-beam tomography system with a reduced size planar detector: a backprojection-filtration reconstruction algorithm as well as numerical and practical experiments. Appl Radiat Isot 65, 1041–1047, doi:10.1016/j.apradiso.2007.01.023 (2007). [PubMed: 17651975]
31. Sanctorum JG et al. Extended imaging volume in cone-beam x-ray tomography using the weighted simultaneous iterative reconstruction technique. Phys Med Biol 66, doi:10.1088/1361-6560/ac16bc (2021).
32. Scarfe WC & Farman AG What is cone-beam CT and how does it work? Dent Clin North Am 52, 707–730, v, doi:10.1016/j.cden.2008.05.005 (2008). [PubMed: 18805225]
33. Tseng HW, Karellas A & Vedantham S Radiation dosimetry of a clinical prototype dedicated cone-beam breast CT system with offset detector. Med Phys 48, 1079–1088, doi:10.1002/mp.14688 (2021). [PubMed: 33501686]
34. Yang K, Kwan AL, Miller DF & Boone JM A geometric calibration method for cone beam CT systems. Med Phys 33, 1695–1706, doi:10.1118/1.2198187 (2006). [PubMed: 16872077]
35. Wu G et al. Estimating scatter from sparsely measured primary signal. J Med Imaging (Bellingham) 4, 013508, doi:10.1117/1.JMI.4.1.013508 (2017). [PubMed: 28401174]
36. Siewerdsen JH et al. A simple, direct method for x-ray scatter estimation and correction in digital radiography and cone-beam CT. Med Phys 33, 187–197, doi:10.1118/1.2148916 (2006). [PubMed: 16485425]
37. Luo Y, Spronk D, Lee Y, Zhou O & Lu J (SPIE Medical Imaging, 2020).
38. <Aarle-Fast and flexible X-ray tomography using the ASTRA toolbox-2016-Optics Express.pdf>.
39. Punnoose J, Xu J, Sisniega A, Zbijewski W & Siewerdsen JH Technical Note: spektr 3.0-A computational tool for X-ray spectrum modeling and analysis. Med Phys 43, 4711, doi:10.1118/1.4955438 (2016). [PubMed: 27487888]
40. Johns PC & Yaffe M Scattered radiation in fan beam imaging systems. Med Phys 9, 231–239, doi:10.1118/1.595076 (1982). [PubMed: 7087909]
41. Phantom Testing: CT (Revised 5-10-22), <https://accreditationsupport.acr.org/support/solutions/articles/11000056197-phantom-testing-ct-revised-5-10-22-> (

42. Pauwels R, Pittayapat P, Sinpitaksakul P & Panmekiate S Scatter-to-primary ratio in dentomaxillofacial cone-beam CT: effect of field of view and beam energy. Dentomaxillofac Radiol, 20200597, doi:10.1259/dmfr.20200597 (2021). [PubMed: 33882256]

43. Kaasalainen T, Ekholm M, Siiskonen T & Kortesniemi M Dental cone beam CT: An updated review. Phys Med 88, 193–217, doi:10.1016/j.ejmp.2021.07.007 (2021). [PubMed: 34284332]

44. Li B et al. in Medical Imaging 2023: Physics of Medical Imaging (2023).

45. Park Y, Alexeev T, Miller B, Miften M & Altunbas C Evaluation of scatter rejection and correction performance of 2D antiscatter grids in cone beam computed tomography. Med Phys 48, 1846–1858, doi:10.1002/mp.14756 (2021). [PubMed: 33554377]

46. Lambert JW et al. Axial or Helical? Considerations for wide collimation CT scanners capable of volumetric imaging in both modes. Med Phys 44, 5718–5725, doi:10.1002/mp.12525 (2017). [PubMed: 28833277]

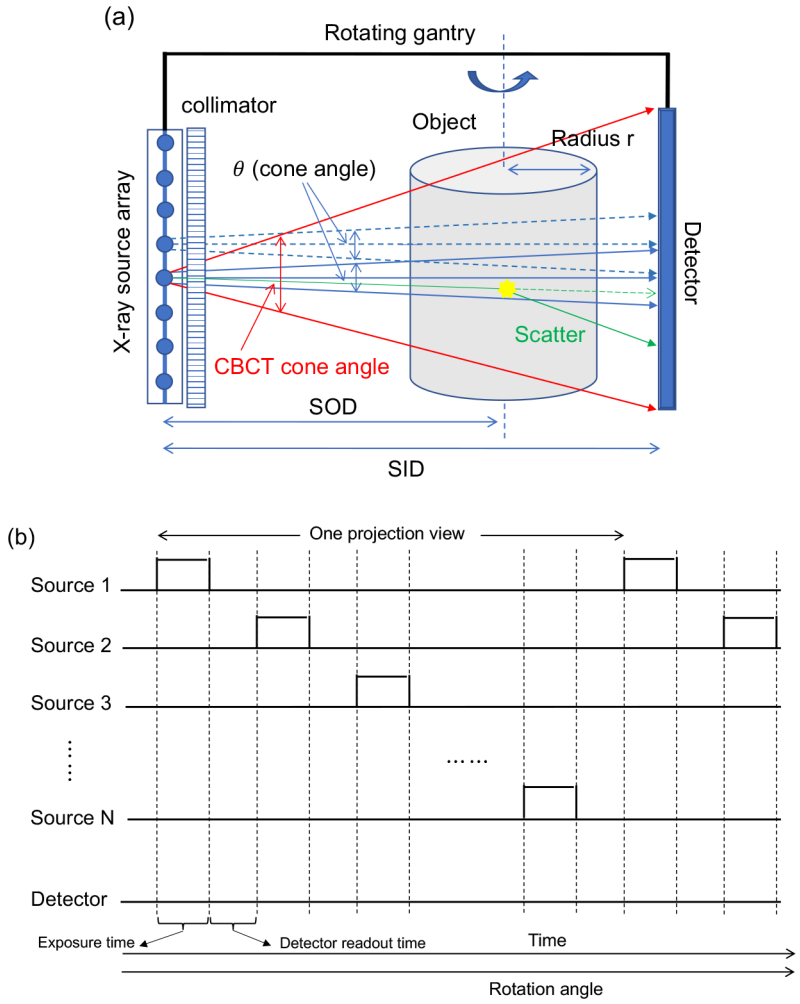

Figure 1:

(a) The proposed ms-CBCT replaces the single X-ray source with a linear CNT X-ray source array with multiple focal spots ("sources") that are aligned along the axial direction of the system. The radiation from each source is collimated to a narrow cone angle. For each X-ray exposure from a focal spot, a segment of the object is imaged and recorded on a corresponding area of the FPD. Any scattered photon received outside this detector area is rejected. (b) For CT imaging the $\boldsymbol{N}_{source}$ number of collimated sources are electronically scanned across the object $\boldsymbol{N}_{view}$ times following the timing diagram shown as the gantry rotates around the object by either 180 + fan angle or 360 degrees as in the conventional CBCT. All together $\boldsymbol{N}_{source} \times \boldsymbol{N}_{view}$ projection images are collected during one full gantry rotation.

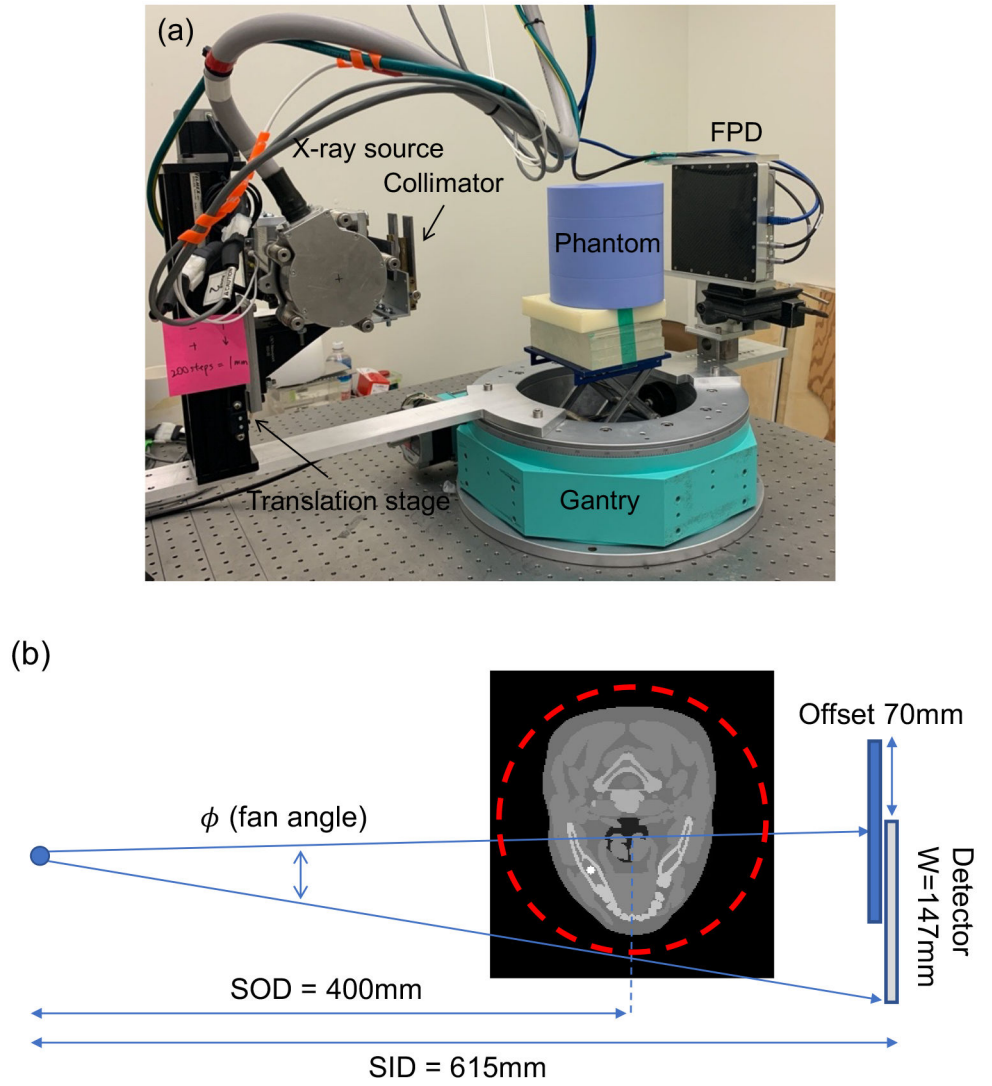

Figure 2:

(a) The benchtop scanner used to evaluate the ms-CBCT design. It consisted of a CNT X-ray source and a flat-panel detector mounted on a rotating gantry. The CNT X-ray source was placed on a motorized translation stage that was moved vertically to experimentally simulate a distributed X-ray source array. An external collimator was used to define the radiation field in both the fan and cone directions. (b) Top view schematic of the offset geometry with a simulated digital head phantom, the red dash circle indicates the effective FOV of the offset geometry.

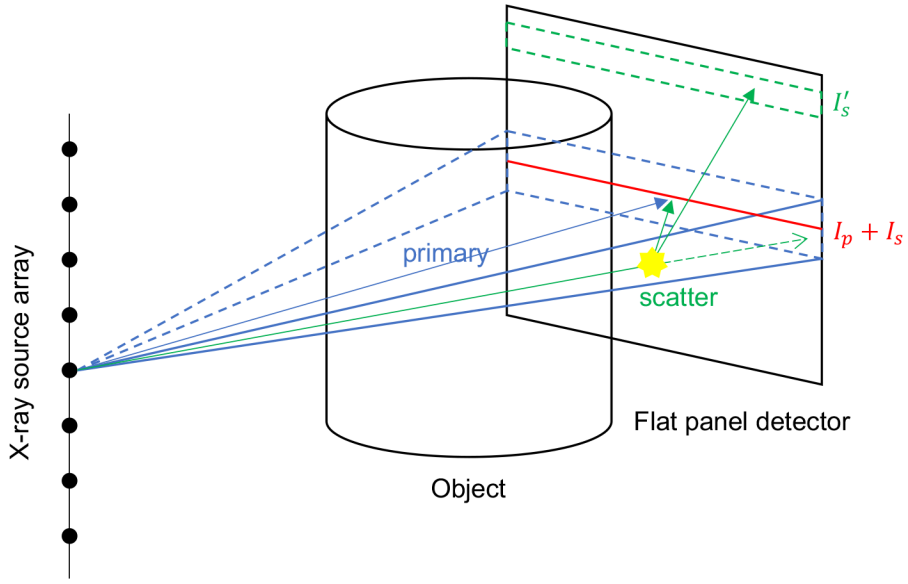

Figure 3:

The schematic diagram of the ASRS method. The blue rectangular region on the detector is illuminated by the primary and scatter photons. The green rectangular region represents the adjacent rows not illuminated by the primary beam.

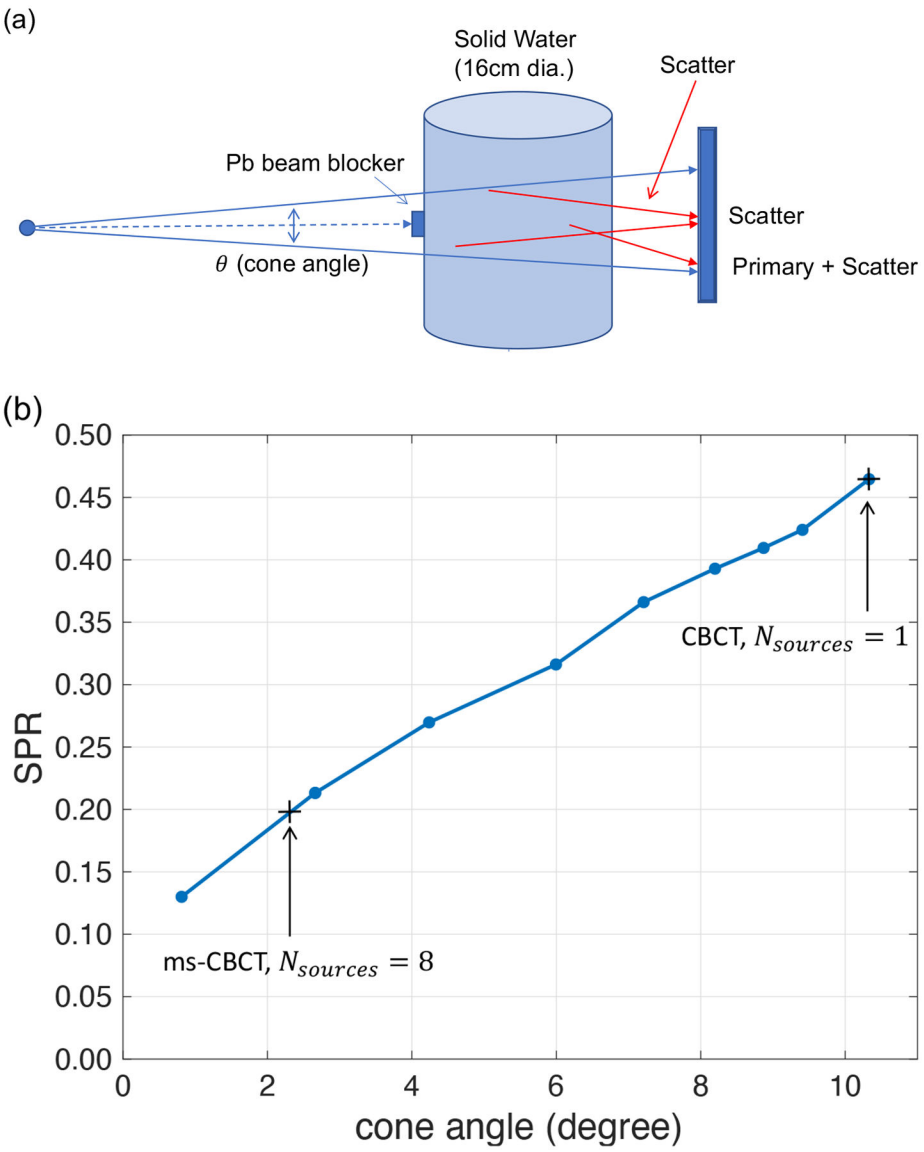

Figure 4:

(a) A schematic showing the experimental set-up for measuring the scatter and the SPR. (b) A plot of the experimentally measured SPR versus the X-ray beam cone angles. The range of cone angles is from 0.8° to 10.3°, and the corresponding total collimation width at the isocenter is from 5.7mm to 72.3mm.

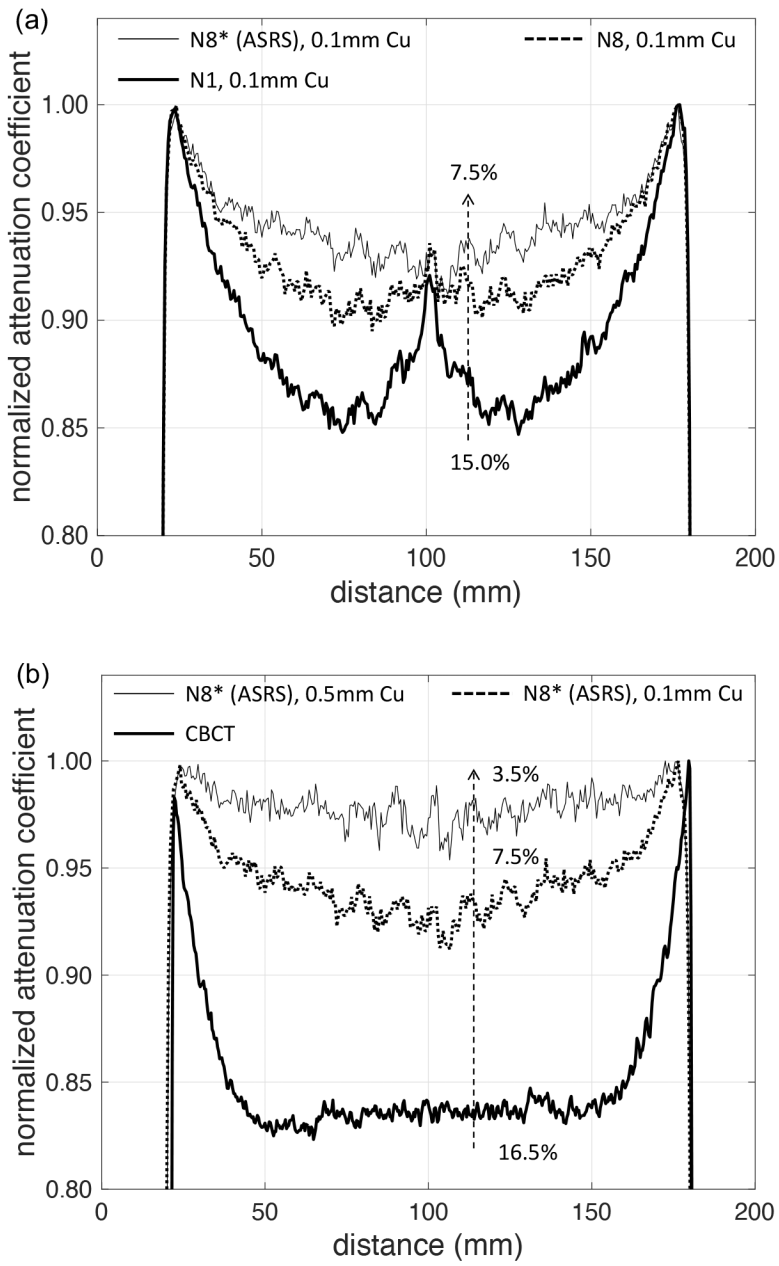

Figure 5:

(a) A plot of the measured linear attenuation coefficient of the 16 cm diameter SolidWater phantom normalized by the maximum value versus the position on the axial plane measured using different ms-CBCT system configurations with 0.1 mm Cu. (b) A line profiles comparison between N8* ms-CBCT with different filtrations and a clinical dental CBCT (3D Accuitomo 170, J. Morita) all operating at the same energy 90 kVp.

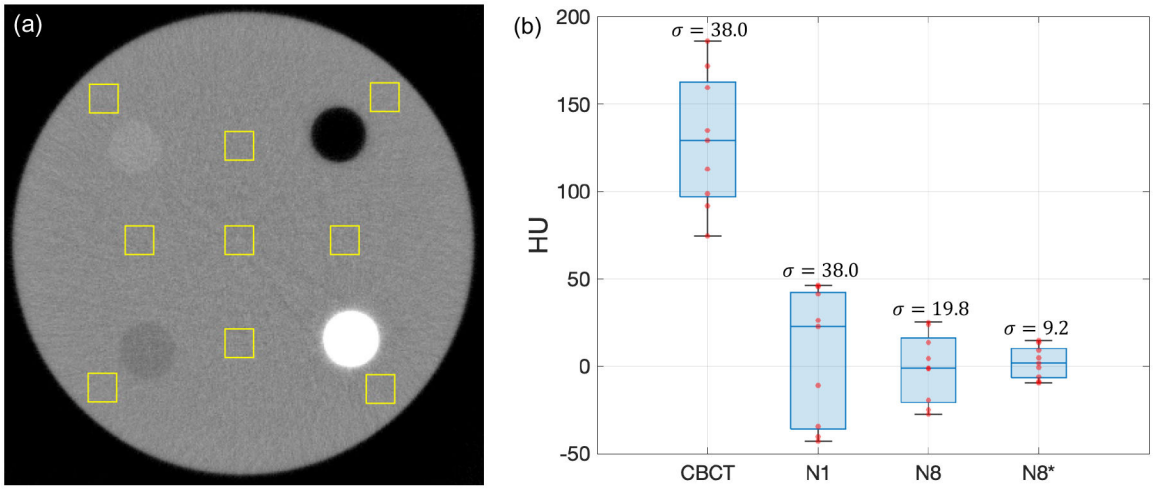

Figure 6:

(a) Nine 10 mm × 10 mm ROIs were chosen for HU spatial uniformity characterization, as shown in the left figure. The image example here is from N8* (ASRS applied) ms-CBCT scanning results. (b) The boxplot figure shows the statistical distribution of all HU mean values from these 9 ROIs of N1, N8, N8* ms-CBCT and clinical CBCT (3D Accuitomo 170, Morita, Japan) scanning results. (Image window: [−1000, 1000]) Note: Grayscale values are currently provided and used instead of HU by the clinical CBCT

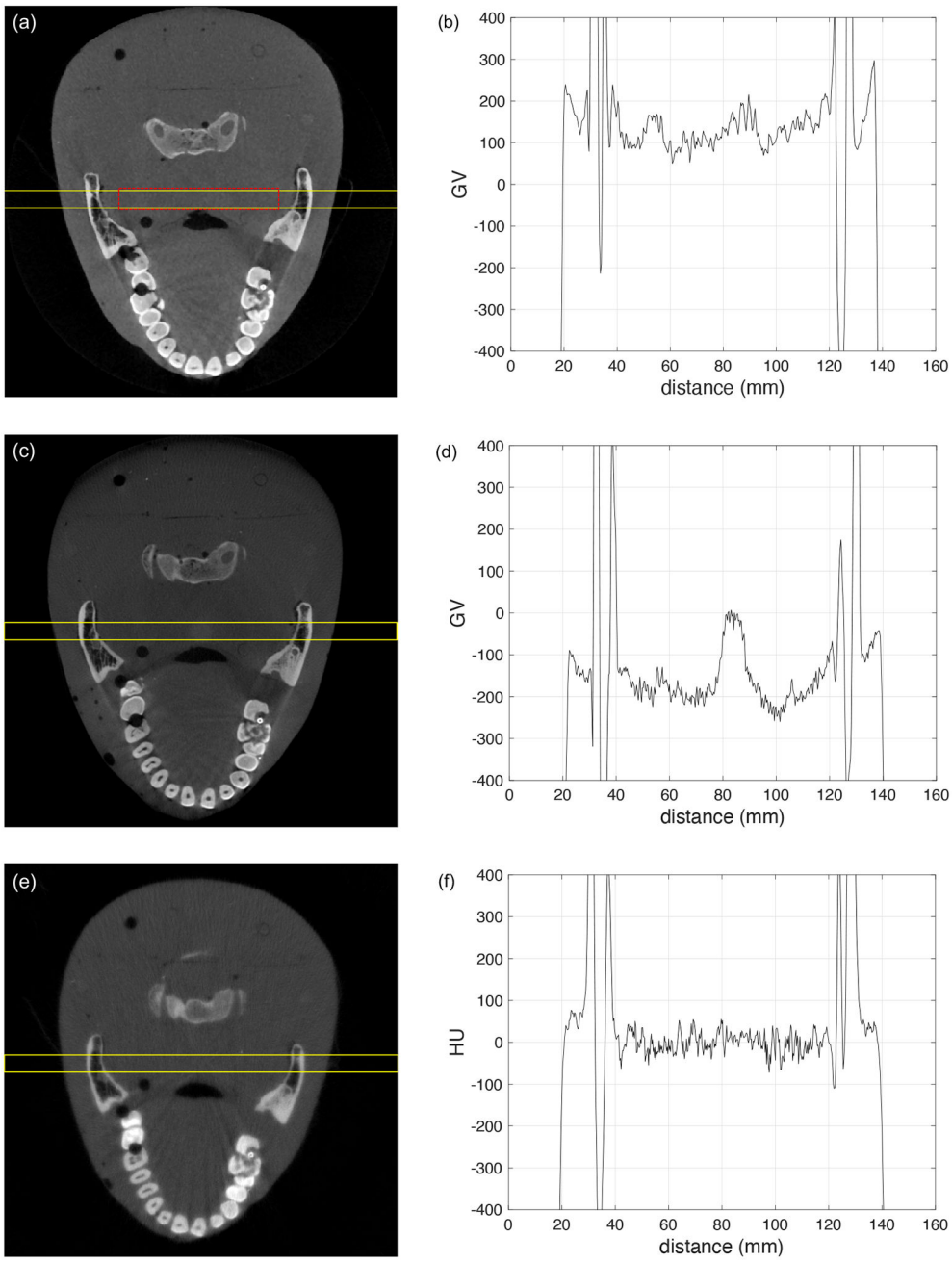

Figure 7:

The line profile from the CT axial slice of the anthropomorphic RANDO phantom imaged using two different clinical dental CBCT scanners (a, b) 3D Accuitomo 170, (c, d) CS9300, and (e, f) the benchtop N8* (ASRS applied) ms-CBCT. Line profiles were averaged over the yellow ROIs shown in (a), (c) and (e). All 3 scanners were operated at 90 kVp. (Image window: [−1000, 3000]).

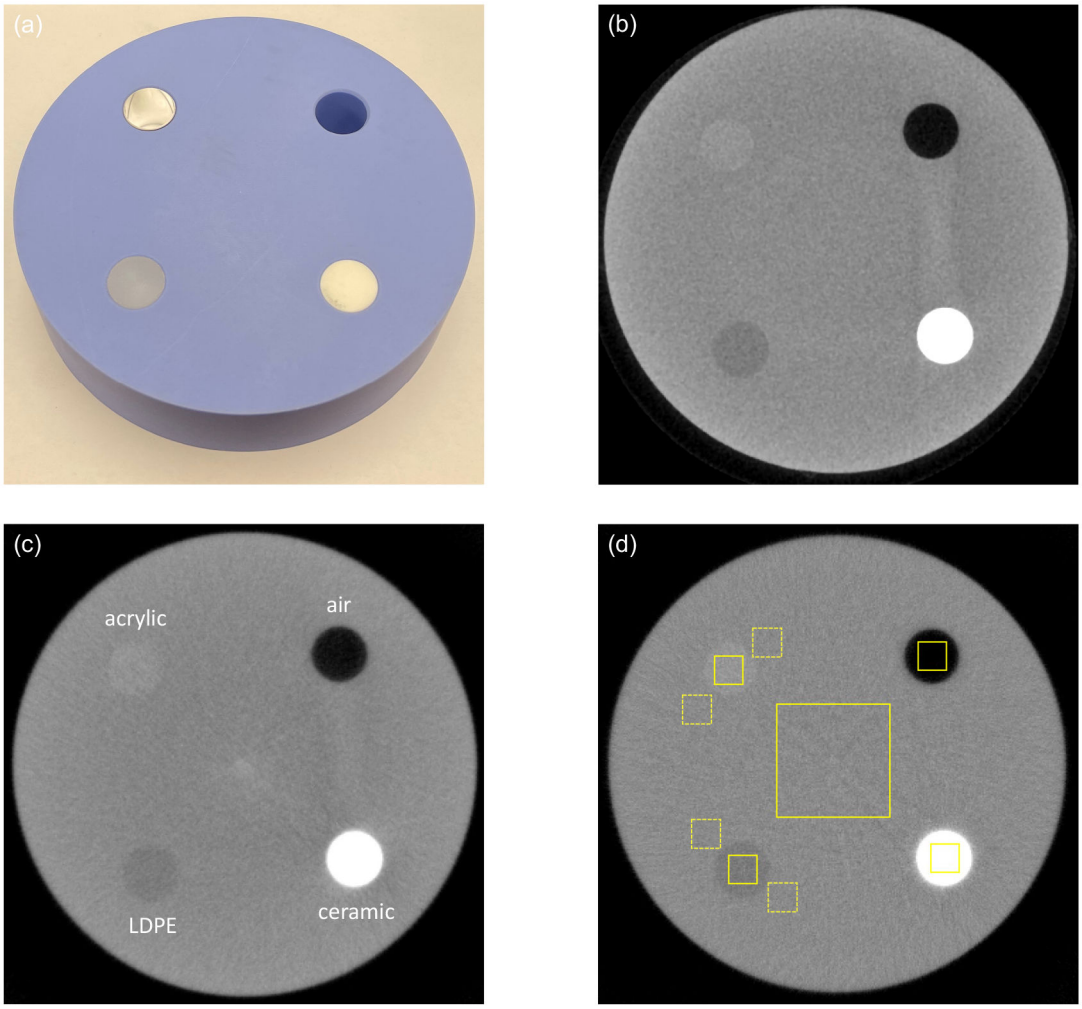

Figure 8:

(a) The homemade contrast phantom containing acrylic, air, ceramic and low-density polyethylene (LDPE) inserts in a 16 cm diameter SolidWater phantom. The reconstructed images of the phantom scanned using (b) a clinical dental CBCT scanner (3D Accuitomo 170, Morita, Japan), the benchtop (c) N1 ms-CBCT (d) N8* (ASRS applied) ms-CBCT. Yellow ROIs in (d) were chosen to measure the HU mean values of different materials. For SolidWater background HU value and standard deviation used in CNR characterization, four yellow dashed ROIs were used to decouple the impact of the cupping effect. (Image window: [−1000, 1000])

Table 1:

Comparison of the CT Hounsfield Unit (HU) values and Greyscale Values (GV's) of the contrast phantom measured from a clinical dental CBCT (3D Accuitomo 170, Morita, Japan), N1 and N8* ms-CBCT for the same FOV and using the same exposure conditions, and a clinical MDCT (SOMATOM Force, Siemens, Germany). The ms-CBCT, clinical CBCT and MDCT were all operated at 90 kVp. Note: (1). Macor is a machinable glass ceramic composed of approximately 55% fluorophlogopite mica and 45% borosilicate glass. (2). Grayscale values are currently provided and used instead of HU by the clinical CBCT.

	Clinical CBCT	**N1 ms-CBCT**	**N8* ms-CBCT**	**Clinical MDCT**
	GV	**HU**	**HU**	**HU**
Acrylic	160.2 ±42.3	57.7 ±50.2	93.1 ± 50.8	123.8 ± 27.1
Air	−867.6 ± 44.1	−856.9 ±43.1	−996.5 ± 12.8	−1023.3 ± 0.9
Macor	1744.2 ± 70.5	1502.3 ± 77.0	2149.2 ± 76.5	2423.3 ±42.1
LDPE	−25.8 ±44.5	−114.5 ± 48.2	−121.7 ± 51.7	−119.6 ±22.0
Water	87.7 ± 44.0	−28.3 ± 56.8	−7.8 ±54.6	15.4 ±24.7
RMSE	316.5	420.1	124.4	